JACS
JOURNAL OF THE AMERICAN CHEMICAL SOCIETY
pubs.acs.org/JACS
Article

Anisotropic Strain Tuning of $L1_0$ Ternary Nanoparticles for Oxygen Reduction

Junrui Li,[#] Shubham Sharma,[#] Kecheng Wei, Zitao Chen, David Morris, Honghong Lin, Cheng Zeng, Miaofang Chi, Zhouyang Yin, Michelle Muzzio, Mengqi Shen, Peng Zhang, Andrew A. Peterson,[*] and Shouheng Sun[*]

Cite This: *J. Am. Chem. Soc.* 2020, 142, 19209−19216

Read Online

ACCESS | Metrics & More | Article Recommendations | Supporting Information

ABSTRACT: Tuning the performance of nanoparticle (NP) catalysts by controlling the NP surface strain has evolved as an important strategy to optimize NP catalysis in many energy conversion reactions. Here, we present our new study on using an eigenforce model to predict and experiments to verify the strain-induced catalysis enhancement of the oxygen reduction reaction (ORR) in the presence of $L1_0$-CoMPt NPs (M = Mn, Fe, Ni, Cu, Ni). The eigenforce model allowed us to predict anisotropic (that is, two-dimensional) strain levels on distorted Pt(111) surfaces. Experimentally, by preparing a series of 5 nm $L1_0$-CoMPt NPs, we could push the ORR catalytic activity of these NPs toward the optimum region of the theoretical two-dimensional volcano plot predicted for $L1_0$-CoMPt. The best ORR catalyst in the alloy NP series we studied is $L1_0$-CoNiPt, which has a mass activity of 3.1 A/mg_{Pt} and a specific activity of 9.3 mA/cm^2 at room temperature with only 15.9% loss of mass activity after 30 000 cycles at 60 °C in 0.1 M $HClO_4$.

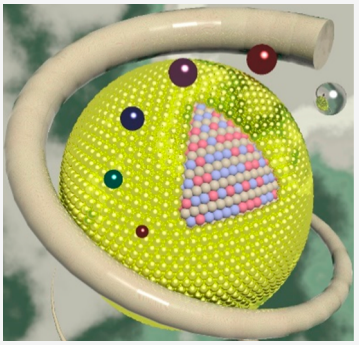

Downloaded via NORTHEASTERN UNIV on December 11, 2022 at 23:12:23 (UTC).
See https://pubs.acs.org/sharingguidelines for options on how to legitimately share published articles.

1. INTRODUCTION

Noble metals, such as Pt, have been widely used in many catalytic applications. To minimize the amount of Pt, Pt-based alloy nanoparticles (NPs) have been intensively studied to improve or even maximize the Pt catalytic performance. Structurally ordered intermetallic alloy NPs have recently evolved as a class of promising candidates due to their well-defined crystal structure, stoichiometry, improved catalytic efficiency, and stability compared to their random alloy counterparts, especially in electrocatalysis.[1−4]

The oxygen reduction reaction (ORR) is an essential electrochemical step in many energy conversion devices, such as fuel cells and metal−air batteries.[5] Alloying Pt with other non-noble metals is a popular strategy to mitigate the overly strong surface Pt binding to key intermediates (*O and *OH) in the ORR catalysis. In many Pt-based random alloy NPs, a dealloying process usually takes place under the electrochemical testing conditions, starting at the surface and subsequently spreading to the core.[6,7] This leads to the structural changes in Pt-alloy NPs (shrinkage in NP size and the evolution of a porous structure), complicating the identification of the active sites and compromising the stability of the alloyed NP catalysts in the aggressive electrochemical testing conditions.

Recent progress has shown that chemically ordered intermetallic Pt-based nanostructures, such as PtPb nanoplates,[8] PtFe NPs,[9,10] PtCo NPs,[11−14] PtNiCo NPs,[15] and PtZn NPs,[16] are highly stable and active ORR catalysts in fuel cell operation conditions.[8,13,16] However, a deep understanding about how to rationally tune and optimize the ORR catalysis of the intermetallic Pt-alloy NPs remains ambiguous. Among the most active ORR catalysts demonstrated in a liquid half-cell study, various mechanisms and models have been proposed to explain the observed high activity,[17−20] yet it is difficult to apply these mechanisms to different systems to assist the catalyst screening. A lanthanide contraction strategy on a series of Pt−lanthanide metal alloys has been reported to largely improve the Pt ORR catalysis via experimental and DFT studies.[21] However, systematic research on the intermetallic Pt alloys with the abundant first-row transition metals (M) is still missing.

While many previous studies have examined the effect of equi-biaxial strain of Pt on its ORR activity, the tetragonal $L1_0$ structure is expected to produce anisotropic strains that are of different magnitudes across different directions of the catalyst surface. To systematically study such anisotropic strain levels, we employed an eigenforce model that we have developed in previous work[22,23] that naturally allows us to create 2D volcano plots. This eigenforce model examines the forces created by the presence of adsorbates and how they interact with applied strains, as shown in Figure 1A and in the Methods Section. To

Received: August 19, 2020
Published: October 30, 2020

ACS Publications
© 2020 American Chemical Society

https://dx.doi.org/10.1021/jacs.0c08962
J. Am. Chem. Soc. 2020, 142, 19209−19216

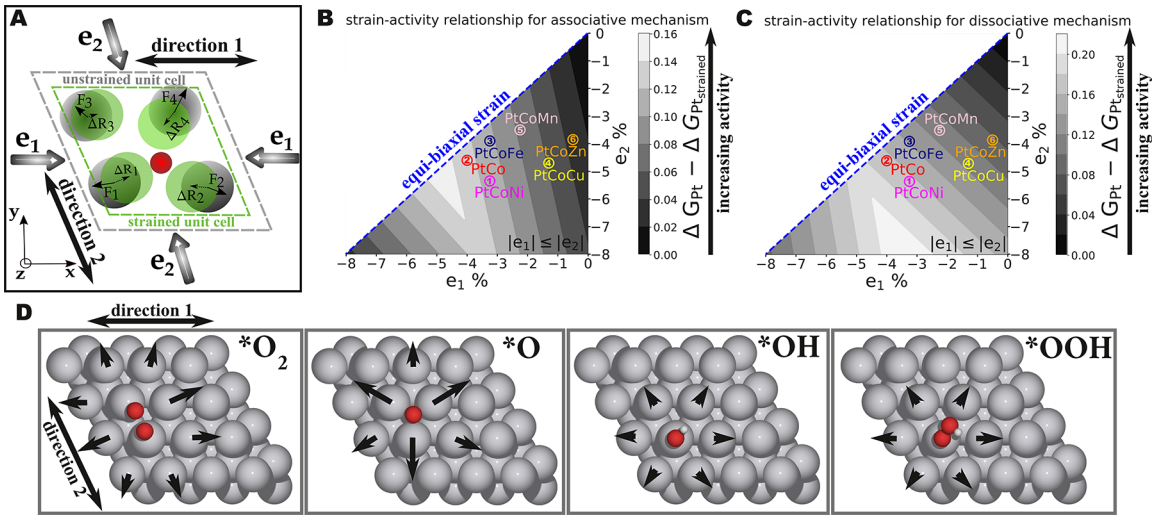

Figure 1. Two-dimensional (2D) strain tuning. (A) Illustration of the in-plane components of the adsorbate-induced eigenforces and the displacement caused by an applied strain (meanings of the symbols are explained in the Methods Section). Calculated 2D volcano plots of strained Pt(111) surfaces using the eigenforce model for (B) the dissociative mechanism and (C) the associative mechanism. The CoMPt (circles) represents $L1_0$-alloyed Pt(111) surfaces in the DFT-optimized lattice constants of their respective ternary $L1_0$-CoMPt alloy. e_1 and e_2 represent the percent strains experienced by the Pt(111) surface in directions 1 and 2, respectively. The numbers on the volcano rank the $L1_0$ strained surfaces in terms of experimentally observed specific activity (SA). (D) In-plane components of eigenforces induced by the geometrically optimized adsorbates on the unstrained Pt(111) surface.

unveil the activity descriptor in intermetallic Pt alloys, we systematically studied a class of ternary $L1_0$-CoMPt (M is Mn, Fe, Ni, Cu, Zn) NPs. As demonstrated in the previous study,[13] $L1_0$-CoPt has been identified as one of the most promising ORR catalysts with high activity and durability in fuel cells. We then synthesized a class of $L1_0$-CoMPt NPs with a size around 5 nm. The ORR study on these $L1_0$-CoMPt NPs showed an activity trend that is consistent with the calculated predictions, indicating that the $L1_0$-CoNiPt ternary alloy, with a mass activity (MA) of 3.1 A/mg_{Pt} and a specific activity (SA) of 9.3 mA/cm^2, is the best ORR catalyst among all the current systems considered.

2. RESULTS AND DISCUSSION

Density Functional Theory (DFT) and Eigenforce Model Calculations. The computational work was performed in two parts. In the first part, we studied the ORR on unstrained Pt using DFT, while the second part focused on employing the eigenforce model to predict the ORR activities on strained surfaces. The two most commonly studied ORR mechanisms, the associative, in which the O−O bond stays intact upon adsorption and protonation, and the dissociative, in which the O−O bond is broken upon adsorption [Table S1, Supporting Information (SI)], were considered throughout (Figure 1B,C). The DFT calculations provided us with stable adsorbed configurations of the ORR intermediates (*O_2, *O, *OH, and *OOH) on an unstrained Pt(111) surface (Figure 1D). The free energies of these stable intermediates were then used to create the free energy landscapes at the ORR equilibrium potential (U = 1.23 V_{RHE}), as shown in Figure S1 (SI). By convention, we treat the step with the maximum uphill free energy change as being the "potential-limiting step" and the potential required to make this step exergonic (i.e., downhill in free energy change) as the "limiting potential". Our calculations showed that the potential-limiting step corresponds to protonation of *OH and *O_2 for dissociative and associative mechanisms, respectively. Destabilizing (i.e., weaken the binding strength) the reaction intermediates with induced compressive strain is a long-known strategy to reduce the limiting potential and improve ORR activity on Pt-based electrocatalyst surfaces.[21,24−27] However, compressive strain beyond an optimum level could render surfaces unfavorable for O_2 adsorption and activation. Hence, a comprehensive search for strain levels that could lead to optimum ORR activity is required.

We used the eigenforce model to explore the ORR activity. This model allows more anisotropic effects to be included[22,28] without employing DFT on strained surfaces, making the search for optimum strain conditions orders of magnitude faster. The model uses adsorbate-induced eigenforces on unstrained surfaces along with strain-induced atomic displacements to determine (both qualitatively and quantitatively) the change in binding strength of an adsorbate. Qualitatively, by introducing an adsorbate to a surface, the neighboring surface atoms could experience forces that pull the surface atoms inward ("negative" eigenforces) or push the atoms away ("positive" eigenforces, as shown in Figure 1A). These eigenforces coupled with the nature of strain (compressive or tensile) could cause stronger or weaker binding of an adsorbate to the surface. If the coupling is inline, i.e., both the applied strain and the induced eigenstress have the same direction, the applied strain stabilizes the adsorbate, resulting in stronger binding. On the other hand, if the applied strain and the induced eigenstress are in opposite directions, the model suggests weaker binding with applied strain. The specifics pertaining to quantification of the change in binding strength with applied strain using the eigenforce model are provided in the Methods Section.

In order to search for near-optimum strain levels for the ORR, we studied surfaces with increasing compressive strain in each of the surface directions (marked as directions 1 and 2 in Figure 1A,D). We varied the strain from 0% to −8% with respect to an unstrained Pt(111) surface in small increments of −0.05% for each direction, resulting in a total of 161 × 161

https://dx.doi.org/10.1021/jacs.0c08962
J. Am. Chem. Soc. 2020, 142, 19209−19216

(=25 921) strained surfaces. The change in binding strength of each ORR intermediate for every strained surface was quantified using the eigenforce model in terms of interaction energies, E_{int}, as explained in the Methods Section. The interaction energies as a function of 2D strain are plotted in Figure S2 (and also provided as CSV files in the SI). Note that more-positive interaction energies suggest a weaker binding strength for an adsorbate. The eigenforces induced by each reaction intermediate on the surface atoms are shown in Figure 1D. We observed that the eigenforces induced by ORR intermediates on the Pt surface atoms are positive, suggesting that applying compressive strain would weaken the binding strength of the ORR intermediates. For all the reaction intermediates except $*O_2$, we observed that the eigenforces induced by each reaction intermediate on the Pt surface are fairly symmetric in all directions. On the other hand, depending on the orientation of $*O_2$, one direction (i.e., the direction along the O_2 bond) experiences higher eigenforces than the other. This suggests that straining the surface in that particular direction effects the binding strength of $*O_2$ more than applying strain in the other direction. For equi-biaxially strained surfaces, all of the $*O_2$ binding sites are identical. However, for anisotropic strained surfaces, we found that $*O_2$ is more stable (i.e., stronger binding strength) in the direction with the larger Pt−Pt distance. For all our calculations, we assumed that, for a particular strained surface, $*O_2$ binds in a way that leads to the most stable configuration. The orientation of the O_2 leads to the anisotropy observed in the volcano plots.

With the interaction energies obtained from the eigenforce model combined with the optimized free energies of ORR intermediates on an unstrained Pt surface, we can estimate the free energy required to make the ORR steps completely exergonic on strained surfaces. This required free energy is equivalent to the theoretical limiting potential when the $O_2(g)$ to $*O_2$ step is exergonic. However, for high compressive strains (i.e., above optimum levels), when the $O_2(g)$ to $*O_2$ step becomes endergonic (i.e., uphill in free energy), the amount of free energy required to make the entire reaction thermodynamically spontaneous equals the free energy change associated with the O_2 activation step plus that of the potential-limiting step for each mechanism. We plot this required change in free energy (with respect to unstrained Pt) for each strained Pt surface to generate 2D volcano plots as shown in Figure 1B,C for associative and dissociative mechanisms, respectively (also provided as CSV files in the SI). At this level of theory, we ignored reaction barriers and assumed that the trends are well-captured by the change in the elementary energetics. Our results suggest that, for the associative mechanism, the minimum limiting potential corresponded to an equi-biaxial compressive strain of ∼5%. The equi-biaxial strain was found to be more beneficial in the associative mechanism, as it allowed for maximum allowable strain from both of the surface directions, resulting in a maximum allowable destabilization of $*O_2$. On the other hand, anisotropic strain with a relatively larger strain along one direction ($e_2 \sim -7\%$) and a smaller one in the other direction ($e_1 \sim -4\%$) was found to be more beneficial for the dissociative mechanism, as it allowed for higher strain in one direction for maximum *OH destabilization while still allowing for O_2 activation. With the eigenforce-model-generated 2D volcano plot, we were able to calculate the ORR activity for any Pt strained surface. We used the above tools to predict the activity trend on Pt in the lattice spacing of $L1_0$-alloyed CoMPt, highlighted as the data points in Figure 1B,C. The change in free energies associated with each elementary step for both mechanisms on $L1_0$ strained surfaces are as shown in Figure S3 of the SI (also provided in Tables S2 and S3). Our calculations suggest that, among all the ternary alloys considered, the strain corresponding to $L1_0$-CoPt and $L1_0$-CoNiPt resulted in the highest ORR activity as observed experimentally. The other $L1_0$-alloyed Pt(111) surfaces were also found to follow the experimental trend fairly well, suggesting that the eigenforce model can be efficiently exploited to screen ORR catalysts without any heavy computational expense.

Preparation and Structural Characterization of Ternary CoMPt NPs. To experimentally study the relationship between the strains and catalytic properties in $L1_0$-CoMPt alloys, we used a facile synthetic method to prepare $L1_0$-CoMPt NPs with sizes around 5 nm. Each of these CoMPt NP samples was first obtained from an organic-phase synthesis and then anchored on a carbon support (C). An annealing followed by an acid post-treatment was used to convert the A1 structure to the $L1_0$ structure and to create a thin Pt shell on the surface (Methods Section and SI). This synthetic method is versatile in tuning the alloy compositions simply by changing the ratio among different metal precursors. As the formation of the $L1_0$ structure requires a specific stoichiometry (typically a ratio of ∼1:1 between nonprecious metal and Pt), we controlled the NP composition to be 1:1:2 of Co:M:Pt. Other compositions, such as $Co_2Ni_1Pt_3$, $Co_1Ni_2Pt_3$, and Ni_1Pt_1, were also obtained (see Figure S4, SI). However, after the same annealing treatment, the $L1_0$ structure was not observed in the $Co_1Ni_2Pt_3$ and Ni_1Pt_1 ones (see Figure S5, SI). The final composition and Pt loading of the C−NPs after acid treatment and annealing were measured by inductively coupled plasma (ICP) analysis (Table S4, SI). The as-synthesized NPs are uniform in size, as shown in the TEM images in Figure 2A−F. After being loaded on the carbon support and annealed at 650 °C for 6 h, $L1_0$ structures were obtained on all CoMPt NPs, as proved by the XRD patterns in Figure 2G, with characteristic peaks at around 24° and 33° for the $L1_0$ structure. Along the (111) direction, the $L1_0$-CoNiPt showed a peak that is at the highest angle (as marked by the vertical line) compared to the other systems, indicating the largest compression along this direction in $L1_0$-CoNiPt among all the systems considered. When Co is partially replaced by M in the ternary CoMPt NPs, the $L1_0$ structure could still be formed, but a minor shift in peaks occurs due to different lattice constants in those $L1_0$ alloys. In Figure S6 (SI), TEM images showed that the C−$L1_0$-NPs were uniformly distributed with no obvious aggregation after the high-temperature annealing. The $L1_0$-CoNiPt was further examined by STEM and elemental mapping. As shown in Figure 3A, the $L1_0$-CoNiPt NP possessed an intermetallic core of alternative Pt layers and Co/Ni layers (as schemed in Figure 3B) that is surrounded by two to three atomic layers of a Pt shell. As Co and Ni have similar atomic weight, it is difficult to distinguish them on the basis of the contrast in the STEM image. The elemental mapping in Figure 3C−F indicates that all three components were uniformly distributed throughout the NP. This is further bolstered by the elemental mapping images in Figure S7 (SI) showing alternative layers of Pt and Co/Ni. A line-scan profile further confirmed the core/shell structure of the $L1_0$-CoNiPt NPs (Figure S8, SI). This $L1_0$ structure can effectively prevent the core Co/Ni components

https://dx.doi.org/10.1021/jacs.0c08962
J. Am. Chem. Soc. 2020, 142, 19209−19216

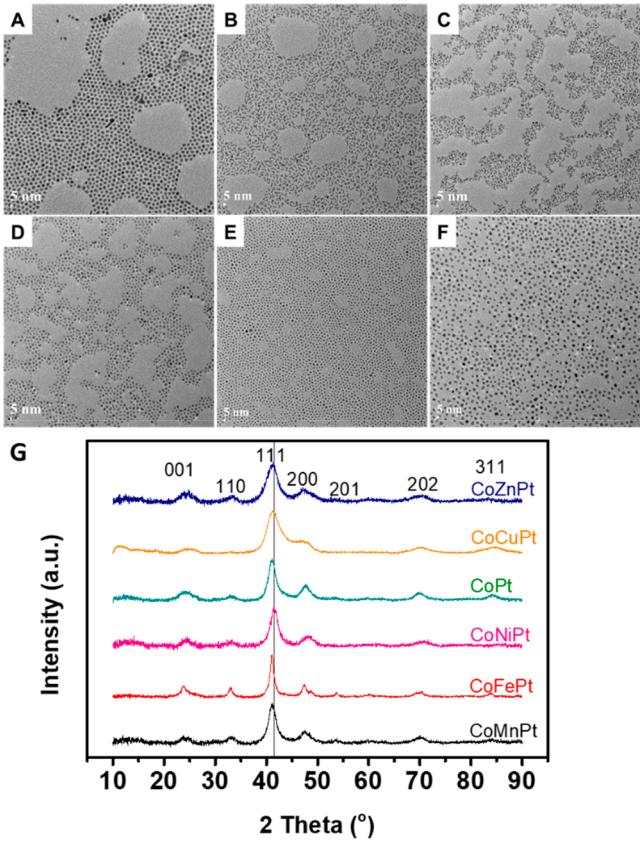

Figure 2. TEM images of as-synthesized (A) CoPt, (B) CoMnPt, (C) CoFePt, (D) CoNiPt, (E) CoCuPt, and (F) CoZnPt. (G) XRD patterns of C−$L1_0$-alloy NPs.

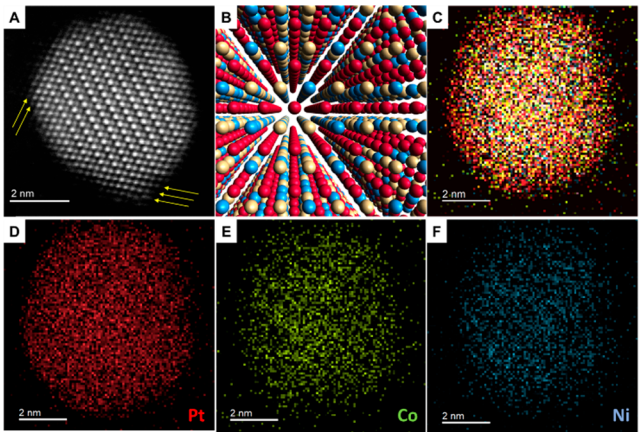

Figure 3. (A) STEM image of a $L1_0$-CoNiPt NP with an atomically thin Pt shell (indicated by yellow arrows). (B) A schematic of $L1_0$-CoNiPt, where Pt is red, Co is yellow, and Ni is blue. Elemental mapping showing (C) an overlapped image of three components and (D) Pt in red, (E) Co in yellow, and (F) Ni in blue.

from being further etched (only the atoms at the very surface are etched away after the acid post-treatment at 60 °C for 24 h). The stabilized $L1_0$-CoNiPt structure maintains Pt surface strain due to the lattice mismatch between the Pt shell and the $L1_0$ core. The local geometric structure of post-treatment $L1_0$-CoNiPt NPs was further checked by EXAFS. As shown in Figure S9 (SI), in both the Co K-edge and Ni K-edge FT-EXAFS, there is a small shoulder peak around 1.6 Å which is assigned to surface oxygen,[29] indicating that some Co and Ni are still near the surface after acid etching, which is consistent with the atomically thin Pt shell observed in STEM imaging. The highest peak around 2.2 Å in Co and Ni graphs is assigned to the Co−Co and Ni−Ni bonds, respectively. The fact that these Co−Co and Ni−Ni peaks are much more intense than the surface oxygen peak proves that the Co and Ni atoms are essentially metallic. The peak around 2.6 Å is assigned to the Co/Ni−Pt bond, indicating that these three components in the NPs are well-alloyed. As shown in Table S5 (SI), the coordination number (CN) of Pt−Pt is 6 and that of Pt−Co/Ni is 5, suggesting that about half of the Pt is bonded to the nonprecious metals. Additionally, the Pt−Pt bond length (2.69 Å) is shorter than that in pure Pt (2.78 Å), indicating the large compression present in the Pt shell.

Oxygen Reduction Reaction (ORR) Catalysis Study. To study the ORR catalysis of C−$L1_0$-CoMPt NPs, the catalysts were first subject to cyclic voltammetry (CV) at room temperature until a stable CV curve was obtained, as shown in Figure S10 (SI). The linear scanning voltammetry (LSV) technique was then used to study the ORR catalytic properties of the catalysts (Figure 4A). Among all the $L1_0$-CoMPt NPs,

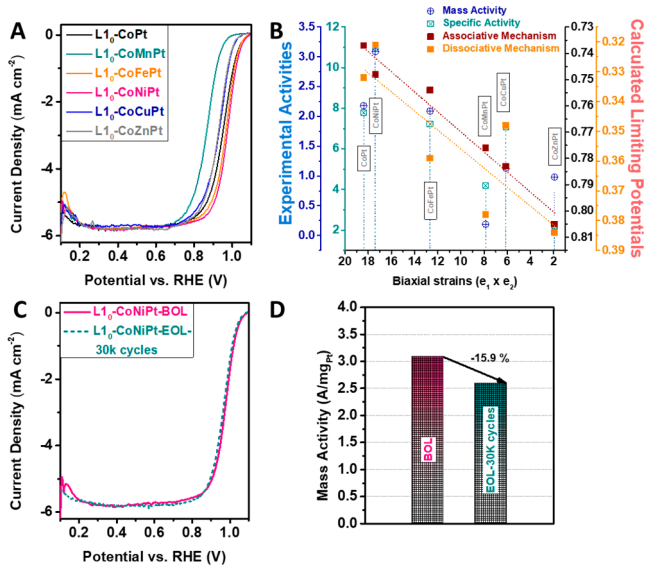

Figure 4. (A) LSV curves of C−$L1_0$-CoPt and $L1_0$-CoMPt NPs (M = Mn, Fe, Co, Ni, Cu, Zn) collected in O_2-saturated 0.1 M $HClO_4$ at room temperature. (B) Plot of experimental activities (MA and SA) and calculated limiting potential from Table S2 (dissociative mechanism) and Table S3 (associative mechanism) (SI) vs biaxial strains $e_1 \times e_2$ of C−$L1_0$-CoPt and C−$L1_0$-CoMPt catalysts. (C) LSV curves of C−$L1_0$-CoNiPt catalyst obtained at the beginning-of-life (BOL) and end-of-life (EOL) in O_2-saturated 0.1 M $HClO_4$. (D) MA loss in C−$L1_0$-CoNiPt after 30 000 cycles. The potentials were cycled between 0.6 and 1.0 V at 60 °C; LSV curves were measured at room temperature.

$L1_0$-CoNiPt showed the highest catalytic performance, with a MA of 3.1 A/mg_{Pt} and a SA of 9.3 mA/cm^2, which is ∼31 times and ∼58 times that of the commercial Pt/C, respectively (as shown in Figure S11, SI). Figure 4B plots the trend in the experimental activities (MA and SA) of $L1_0$-CoPt and $L1_0$-CoMPt catalysts vs the 2D biaxial strains ($e_1 \times e_2$), which is consistent with the theoretically observed trend in the ORR activity with 2D biaxial strains. The durability test of $L1_0$-CoNiPt was conducted by cycling the potential between 0.6 and 1.0 V at 60 °C, a fuel-cell-relevant temperature. Then the

https://dx.doi.org/10.1021/jacs.0c08962
J. Am. Chem. Soc. 2020, 142, 19209−19216

LSV curve was measured again at room temperature for comparison. As shown in Figure 4C,D, only a negligible shift in the LSV curve and a slight drop of 15.9% in the MA was observed after 30 000 cycles, demonstrating that the $L1_0$ structure provides high activity and durability to Pt catalysis. On the basis of the ICP analysis, the composition of $L1_0$-CoNiPt after the durability test is $Co_{23.7}Ni_{20.4}Pt_{55.9}$ with no obvious change compared to the composition before the test (Table S4, SI). As the nonprecious metal components can be well-stabilized under the very aggressive electrochemical condition at 60 °C, the compressive strain in the Pt surface can be well-maintained for ORR catalysis.

3. CONCLUSIONS

In conclusion, we used DFT calculations and an eigenforce model to describe the relationship between the limiting potential and the 2D lattice compression in strained Pt surfaces. The theoretically predicted trend of the $L1_0$-CoMPt catalysts was consistent with experimentally observed ORR activities of 5 nm $L1_0$-CoMPt NPs. An anisotropic compressive strain was introduced by alloying various first-row transition metals (M) with Pt in the ternary NPs, which were well-stabilized by the $L1_0$ structure under the aggressive electrochemical testing conditions. As the computational study suggested that $L1_0$-CoNiPt has the near-optimum strain levels, a fine control in the synthesis resulted in the best ORR catalytic performance for $L1_0$-CoNiPt among a series of $L1_0$-CoMPt catalysts. $L1_0$-CoNiPt showed a MA of 3.1 A/mg_{Pt} and a SA of 9.3 mA/cm^2 with less than a 16% drop in MA after 30 000 potential cycles between 0.6 and 1.0 V at 60 °C, demonstrating its great promise for fuel cell applications. Combining theory and experiments, this study provides insights about finely tuning the catalytic activity in intermetallic NPs with well-defined structures and compositions.

4. METHODS SECTION

Chemicals and Materials. All chemicals were used without purification. $Pt(acac)_2$ (acac = acetylacetonate) (98%) was purchased from Strem Chemical, Inc. $Mn(acac)_2$, $Fe(acac)_3$ (99%), $Co(acac)_2$ (>97%), $Ni(acac)_2$ (95%), $Cu(acac)_2$ (97%), $Zn(acac)_2$ hydrate, oleylamine (OAm) (70%), borane–*tert*-butylamine (BBA) complex, and Nafion (5% in a mixture of 2-propanol and water) were purchased from Sigma-Aldrich. The commercial Pt catalyst (20% mass loading on carbon, Pt particle diameter at 2.5–3.5 nm) was purchased from Fuel Cell Store.

Preparation of 5 nm CoMPt Nanoparticles (M = Mn, Fe, Ni, Cu, Zn). Portions of 0.5 mmol of $Pt(acac)_2$, 0.28 mmol of $Co(acac)_2$, and 0.28 mmol of $M(acac)_x$ (x = 2 when M is Mn, Co, Ni, Cu or Zn, whereas x = 3 when M = Fe) were mixed with 20 mL of OAm in a four-necked reaction flask. A 0.56 mmol portion of BBA was added to the mixture before the reaction was heated to 120 °C under nitrogen protection for 30 min. The heating was then ramped to 300 °C at a rate of 5 °C/min and kept at this temperature for 1 h. The mixture was cooled to room temperature and mixed with 10 mL of hexanes to be transferred evenly to two centrifuge tubes. About 35 mL of ethanol was added to each centrifuge tube, which was then centrifuged at 8500 rpm for 8 min. The clear supernatant was disposed of and the NP product that adhered to the wall of the centrifuge tubes was washed with a mixture of hexanes (10 mL) and ethanol (70 mL) two more times. The final product was redispersed in hexanes (~20 mL) for further use.

Preparation of Carbon-Supported Intermetallic $L1_0$-CoMPt. Ketjen-300J carbon was suspended in hexane under sonication for 10 min, and then a certain amount of CoMPt NPs dispersion was added dropwise into the carbon suspension and sonicated for 1 h. The Pt loading amount was maintained at 10–15 wt %. The carbon-supported (C–CoMPt) NPs suspension was left standing still until the solid precipitated out. The clear hexane layer was removed with a pipet and the solid was dried out under a gentle flow of nitrogen. C–CoMPt NPs were then annealed under 95% Ar + 5%H_2 at 650 °C for 6 h to form an intermetallic $L1_0$ structure in the NPs, followed by a acid post-treatment with 0.1 M $HClO_4$ at 60 °C overnight. The acid-etched C–NPs were then annealed under 95% Ar + 5%H_2 at 400 °C for 2 h to obtain the final catalysts for further characterization. This method was adopted from our previous publications, which showed that as-synthesized A1-structured NPs with a specific composition could be converted into the $L1_0$ structure through annealing treatment. An acid post-treatment followed by annealing helped to form a smooth Pt shell surrounding the $L1_0$ core.[10,13]

Characterization. TEM images were acquired from a Philips FEI CM20 transmission electron microscope (TEM) (200 kV) and JEOL 2100F HR-TEM (200 kV). X-ray diffraction (XRD) was recorded on the Bruker AXS D8-Discovery high-resolution X-ray diffractometer with Cu Kα radiation (λ = 1.5418 Å). Compositions of the materials were calculated from the ICP results obtained on a JY2000 Ultrace ICP atomic emission spectrometer equipped with a JY AS 421 autosampler and 2400 g/mm holographic grating. An aqueous suspension of samples was drop-cast onto the lacey carbon grid and then allowed to dry under ambient conditions before conducting HAADF-STEM and elemental mapping tests. HAADF-STEM images were taken from an aberration-corrected FEI Titan 80–300 kV TEM/STEM microscope at an accelerating voltage of 300 kV, with a probe convergence angle of 30 mrad and a large inner collection angle of 65 mrad to provide a nominal image solution of 0.7 Å. Energy-dispersive X-ray spectroscopy (EDX) data of the samples were acquired using an aberration-corrected JEOL NEOARM microscope with dual large-angle EDX-SDD detectors at Oak Ridge National Laboratory.

Pt L_3-edge and Co and Ni K-edge XAFS data were collected from the CLS@APS (Sector 20-BM) beamline at the Advanced Photon Source (operating at 7.0 GeV) of Argonne National Laboratories, Chicago, IL. Powdered samples were measured in fluorescence mode simultaneously with Pt, Co, and Ni foil references. All measurements were conducted at room temperature and ambient pressure. EXAFS data were transformed and normalized into k- and R-space using the Athena program following conventional procedures. A k weighting of 2 was used to obtain all FT-EXAFS spectra. A k-range of 2.3–11.9 $Å^{-1}$ and an R-range of 1.3–3.3 Å were used to obtain the Pt FT-EXAFS spectra. Self-consistent multiple-scattering calculations were performed using the FEFF6 program to obtain the scattering amplitudes and phase-shift functions used to fit various scattering paths with the Artemis program. In the fitting, the E_0 values were correlated together to minimize the number of independent values, allowing reliable fitting results to be obtained.

Catalyst Ink Preparation and Electrochemical Measurement. Catalyst ink for electrochemical study was prepared by sonicating 1 mg of C–NPs with 800 μL of ultrapure water, 200 μL of 2-propanol, and 10 μL of Nafion solution (5 wt %) for 1 h. A 20 μL aliquot of the catalyst ink was then drop-casted on a glassy carbon rotating disk electrode (5 mm in diameter) for the electrochemical study using an Autolab 302 potentiostat. Ag/AgCl (4 M KCl) and graphite rod were used as the reference electrode and counter electrode, respectively. C-loaded NPs catalyst was first subjected to scans between 0 and 1.2 V vs RHE using cyclic voltammetry (CV) at 100 mV/s in N_2-saturated 0.1 M $HClO_4$ at room temperature until a stable curve was obtained (typically 50 cycles). Then, at the room temperature, the ORR performance was evaluated by using the linear scanning voltammetry (LSV) technique at a scanning rate of 20 mV/s in O_2-saturated 0.1 M $HClO_4$ with the RDE rotating at 1600 rpm. Accelerated durability tests (ADT) of the catalysts were conducted at 60 °C by cycling the potential between 0.6 and 1.0 V using CV at 100 mV/s.

Computational Methods. The electronic structure calculations were performed using the GPAW (grid-based projector-augmented wave)[30,31] method with the atomic systems created and manipulated in ASE (atomic simulation environment).[32] We used an RPBE (Perdew–Burke–Ernzerhof) exchange–correlation functional[33] with

https://dx.doi.org/10.1021/jacs.0c08962
J. Am. Chem. Soc. 2020, 142, 19209–19216

a plane wave basis set of 450 eV plane wave cutoff and a 4 × 4 × 1 *k*-point mesh. To model the surfaces, we used 3 × 4 as well as 4 × 4 supercells with four atomic layers. To capture all of the significant eigenforces, a 4 × 4 supercell was used for systems containing $*O_2$ and *O, while a 3 × 4 supercell was used for systems with *OH and *OOH. A vacuum of 15 Å was used in the *z*-direction. The DFT calculations for surface energetics were only performed on unstrained Pt(111) surfaces, while the eigenforce model, introduced in the next section, was used for the strained systems. As a refinement of the eigenstress model previously reported,[23] the eigenforce model[22] was shown to be a promising tool to intuitively characterize and quantify the binding behavior of an adsorbate with applied strain. Although the presence of subsurface non-Pt elements could affect the ORR activity by altering the binding strength of reaction intermediates, it is known that for a Pt overlayer of about two or more, the effect of strain is dominant.[22,34] Hence, for simplicity, we only focus on strain effects. Sharma et al.[22] have shown that the binding energy predictions of the eigenforce model follow the same trends as observed through DFT calculations on strained Pt surfaces, suggesting that the eigenforce model can be considered as an effective tool for fast screening of ORR catalysts without employing computationally expensive DFT calculations on strained surfaces.

The RPBE-optimized lattice constants for unstrained Pt, $L1_0$-CoNiPt, $L1_0$-CoFePt, $L1_0$-CoCuPt, $L1_0$-CoPt, $L1_0$-CoMnPt, and $L1_0$-CoZnPt (listed in Table S6, SI) were used to simulate unstrained Pt as well as strained surfaces in the lattice spacing of $L1_0$ alloys. The *k*-point mesh used for lattice constant optimization was 8 × 8 × 8. The strained Pt surfaces were created by applying strain to the unstrained supercell in the periodic directions (marked 1 and 2 in Figure 1A) and scaling the positions of the atoms to the new supercell.

The most stable adsorbed configurations of the reaction intermediates on unstrained Pt were obtained by employing DFT to perform geometric optimizations on the top three layers of the slab and the adsorbate while constraining (or fixing) the bottom-most layer of the slab. The geometries corresponding to the lowest potential energy were used for each reaction intermediate. All geometry optimizations in this work were carried out until the force on each unconstrained atom reached below 0.05 eV/Å. The thermochemistry module[32] available in ASE was employed to convert the potential energies to free-energies where gas-phase species were treated in the ideal-gas limit and the adsorbates were treated in the harmonic limit. The free energies associated with the gas-phase adsorbates were obtained using the RPBE free energies of H_2O and H_2 combined with the experimental reaction free energy of 2.46 eV for the formation of $^1/_2O_2$ and H_2 from H_2O. We employed the CHE (computational hydrogen electrode) model[35] to obtain the energetics involved in a $(H^+ + e^-)$ transfer. In the CHE model, the chemical potential of gaseous hydrogen $(\frac{1}{2}\mu[H_2])$ is considered equal to the chemical potential of the proton−electron pair $(\mu[H^+] + \mu[e^-])$ at 0 V_{RHE}. The free energy landscapes for unstrained Pt(111) surfaces were created at 300 K by adding $\Delta G_U = -eU$ to adjust the reaction potential relative to 0 V_{RHE}. Here, U represent the working electrode potential on the RHE scale.

In order to calculate the eigenforces on unstrained Pt(111) surfaces, we started off by relaxing a bare Pt(111) surface while keeping the bottom-most Pt layer fixed to its bulk lattice. Once relaxed, we added an adsorbate to the surface while fixing the relaxed Pt slab. The adsorbate is then allowed to relax on the fixed slab, which induces forces on the neighboring atoms of the adsorbate. The induced forces on the slab atoms were then obtained using an atomic force call to the electronic structure calculator. We convert these forces to explicit interaction energies as discussed in the next section.

Eigenforce Model Used to Predict ORR Volcano Plots. A modification of the eigenstress model,[23] the eigenforce model, was used to predict 2D volcano plots for the ORR, as shown in Figure 1B,C. According to the eigenstress model,[23] a perturbation created on a subdomain of a continuous body can induce an eigenstress σ^* (a tensor) on the surface boundary. The adsorbate can either pull the neighboring atoms inward, creating a negative eigenstress, or push the atoms outward, creating a positive eigenstress. The coupling of this induced eigenstress and the nature of the applied strain can be used to predict the effect of strain on adsorbate binding. At any arbitrary applied external strain ϵ^0 (a tensor), the binding energy of an adsorbate can be decomposed as

$$E_b(\epsilon^0) = E_b(0) + E_{int}(\epsilon^0,\sigma^*)$$

where $E_b(\epsilon^0)$ is the total binding energy of the adsorbate when the slab experiences an applied strain of ϵ^0 (a tensor), $E_b(0)$ is the binding of an adsorbate at zero applied strain, and $E_{int}(\epsilon^0,\sigma^*)$ is defined as the interaction potential energy of the applied external strain with the induced eigenstress. The interaction energy computed over a subdomain of volume V in the limit of linear elasticity $E_{int}(\epsilon^0,\sigma^*)$ is described as

$$E_{int} = -\int_V \sum_{i,j} [\epsilon_{ij}^0(x)\ \sigma_{ij}^*(x)]dx$$

Here, ϵ_{ij}^0 and σ_{ij}^* are the tensorial components of ϵ^0 and σ^*, respectively. On the basis of the nature of coupling between the eigenstress and the applied strain, the eigenstress model can predict the qualitative effect on the binding of an adsorbate. If the coupling is inline, i.e., both the applied strain and the induced eigenstress have the same sign, the interaction energy becomes negative and the model predicts stronger binding with applied strain. On the other hand, if the applied strain and the induced eigenstress are in opposite directions, the model suggests weaker binding with applied strain. Note that more positive binding energy implies weaker binding. Here, compressive strain is considered negative while a tensile strain is positive. The eigenstress model has proven to be an impressive tool in predicting the "qualitative" behavior of an adsorbate with applied strain.[23,22] However, it faces limitations when dealing with "quantitative" prediction due to the difficulty in transference of continuum properties, like stress and strain, to atomic modeling. The eigenforce model overcomes this issue by replacing eigenstress and strain with eigenforces and atomic displacements, respectively. This makes the eigenforce model easy to quantify. In the eigenforce model, the interaction energy can be obtained through

$$E_{int}(F,R) = -\sum_{i\in S} \int F_i\ dR_i$$

where R_i is the Cartesian coordinate of the atom i and F_i is the force on the corresponding surface atom induced by relaxing an adsorbate on a fixed unstrained surface (S). Further simplification of the interaction energy is assumed by considering the eigenforces to remain constant with strain. This results in the interaction energy to be written as

$$E_{int}(F,R) = -\sum_{i\in S} F_i\Delta R_i$$

Here, ΔR_i is the change in the Cartesian coordinates of an atom (due to applied external strain). Ideally the eigenforce will not remain constant with strain. If the forces and displacement are inline, the forces will tend to decrease with increasing strain. On the other hand, if the forces are in the opposite direction of the atomic displacement, the forces will tend to increase with more strain. The above simplification introduces a systematic second-order error into the equation. The interaction energy provides an estimate of the shift in the binding energy of each adsorbate with applied strain. The shift in the predicted binding energies obtained through the eigenforce model can be used to create free energy landscapes on strained surfaces. It has been shown previously by Sharma et al.[22] that the eigenforce model was able to predict limiting potentials for ORR via both dissociative and associative mechanisms on strained surfaces within ∼0.1 eV difference of DFT calculations. Thus, we can estimate the free energy landscape of a reaction with reasonable accuracy using atomic forces and displacements without performing exclusive DFT calculations on strained surfaces.

https://dx.doi.org/10.1021/jacs.0c08962
J. Am. Chem. Soc. 2020, 142, 19209−19216

■ ASSOCIATED CONTENT

Supporting Information

The Supporting Information is available free of charge at https://pubs.acs.org/doi/10.1021/jacs.0c08962.

Figures S1−S1 and Tables S1−S6 (PDF)
Interaction energy vs 2D strain for O (CSV)
Interaction energy vs 2D strain for O_2 (CSV)
Interaction energy vs 2D strain for OH (CSV)
Interaction energy vs 2D strain for OOH (CSV)
Required ΔG vs 2D strain for the dissociative mechanism (CSV)
Required ΔG vs 2D strain for the associative mechanism (CSV)

■ AUTHOR INFORMATION

Corresponding Authors

Andrew A. Peterson − *School of Engineering, Brown University, Providence, Rhode Island 02912, United States;* orcid.org/0000-0003-2855-9482; Email: Andrew_Peterson@brown.edu

Shouheng Sun − *Department of Chemistry, Brown University, Providence, Rhode Island 02912, United States;* orcid.org/0000-0002-4051-0430; Email: ssun@brown.edu

Authors

Junrui Li − *Department of Chemistry, Brown University, Providence, Rhode Island 02912, United States;* orcid.org/0000-0002-4386-1199

Shubham Sharma − *School of Engineering, Brown University, Providence, Rhode Island 02912, United States*

Kecheng Wei − *Department of Chemistry, Brown University, Providence, Rhode Island 02912, United States*

Zitao Chen − *Center for Nanophase Materials Sciences Division, Oak Ridge National Laboratory, Oak Ridge, Tennessee 37831, United States; The Wallace H. Coulter Department of Biomedical Engineering, Georgia Institute of Technology and Emory University, Atlanta, Georgia 30332, United States*

David Morris − *Department of Chemistry, Dalhousie University, Halifax, Nova Scotia B3H 4R2, Canada*

Honghong Lin − *Department of Chemistry, Brown University, Providence, Rhode Island 02912, United States*

Cheng Zeng − *School of Engineering, Brown University, Providence, Rhode Island 02912, United States*

Miaofang Chi − *Center for Nanophase Materials Sciences Division, Oak Ridge National Laboratory, Oak Ridge, Tennessee 37831, United States;* orcid.org/0000-0003-0764-1567

Zhouyang Yin − *Department of Chemistry, Brown University, Providence, Rhode Island 02912, United States*

Michelle Muzzio − *Department of Chemistry, Brown University, Providence, Rhode Island 02912, United States*

Mengqi Shen − *Department of Chemistry, Brown University, Providence, Rhode Island 02912, United States;* orcid.org/0000-0001-9265-6784

Peng Zhang − *Department of Chemistry, Dalhousie University, Halifax, Nova Scotia B3H 4R2, Canada;* orcid.org/0000-0003-3603-0175

Complete contact information is available at: https://pubs.acs.org/10.1021/jacs.0c08962

Author Contributions

[#]J.L. and S.S. contributed equally to this work.

Notes

The authors declare no competing financial interest.

■ ACKNOWLEDGMENTS

The work was supported by the US Department of Energy (DOE), Energy Efficiency and Renewable Energy, Fuel Cell Technologies Office. Los Alamos National Laboratory is operated by Los Alamos National Security, LLC, under contract no. DE-AC52-06NA25396. This research used resources of the Advanced Photon Source, an Office of Science User Facility operated for the DOE Office of Science by Argonne National Laboratory, and was supported by the US DOE, under contract no. DE-AC02-06CH11357, and the Canadian Light Source and its funding partners. The HAADF-STEM study was conducted at Oak Ridge National Laboratory's Center for Nanophase Materials Sciences, which is a DOE Office of Science User Facility.

■ REFERENCES

(1) Li, J.; Sun, S. Intermetallic Nanoparticles: Synthetic Control and Their Enhanced Electrocatalysis. *Acc. Chem. Res.* **2019**, *52* (7), 2015−2025.

(2) Xiao, W.; Lei, W.; Gong, M.; Xin, H. L.; Wang, D. Recent Advances of Structurally Ordered Intermetallic Nanoparticles for Electrocatalysis. *ACS Catal.* **2018**, *8* (4), 3237−3256.

(3) Gamler, J. T. L.; Ashberry, H. M.; Skrabalak, S. E.; Koczkur, K. M. Random Alloyed versus Intermetallic Nanoparticles: A Comparison of Electrocatalytic Performance. *Adv. Mater.* **2018**, *30* (40), 1801563.

(4) Yan, Y.; Du, J. S.; Gilroy, K. D.; Yang, D.; Xia, Y.; Zhang, H. Intermetallic Nanocrystals: Syntheses and Catalytic Applications. *Adv. Mater.* **2017**, *29* (14), 1605997.

(5) Song, C.; Zhang, J. Electrocatalytic Oxygen Reduction Reaction. In *PEM Fuel Cell Electrocatalysts and Catalyst Layers: Fundamentals and Applications*; Springer London: London, 2008; pp 89−134.

(6) Cui, C.; Gan, L.; Heggen, M.; Rudi, S.; Strasser, P. Compositional Segregation in Shaped Pt Alloy Nanoparticles and Their Structural Behaviour during Electrocatalysis. *Nat. Mater.* **2013**, *12* (8), 765−771.

(7) Baldizzone, C.; Gan, L.; Hodnik, N.; Keeley, G. P.; Kostka, A.; Heggen, M.; Strasser, P.; Mayrhofer, K. J. J. Stability of Dealloyed Porous Pt/Ni Nanoparticles. *ACS Catal.* **2015**, *5* (9), 5000−5007.

(8) Feng, Y.; Shao, Q.; Lv, F.; Bu, L.; Guo, J.; Guo, S.; Huang, X. Intermetallic PtBi Nanoplates Boost Oxygen Reduction Catalysis with Superior Tolerance over Chemical Fuels. *Adv. Sci.* **2020**, *7* (1), 1800178.

(9) Li, Q.; Wu, L.; Wu, G.; Su, D.; Lv, H.; Zhang, S.; Zhu, W.; Casimir, A.; Zhu, H.; Mendoza-Garcia, A.; Sun, S. New Approach to Fully Ordered Fct-FePt Nanoparticles for Much Enhanced Electrocatalysis in Acid. *Nano Lett.* **2015**, *15* (4), 2468−2473.

(10) Li, J.; Xi, Z.; Pan, Y. T.; Spendelow, J. S.; Duchesne, P. N.; Su, D.; Li, Q.; Yu, C.; Yin, Z.; Shen, B.; Kim, Y. S.; Zhang, P.; Sun, S. Fe Stabilization by Intermetallic L10-FePt and Pt Catalysis Enhancement in L10-FePt/Pt Nanoparticles for Efficient Oxygen Reduction Reaction in Fuel Cells. *J. Am. Chem. Soc.* **2018**, *140* (8), 2926−2932.

(11) Wang, D.; Xin, H. L.; Hovden, R.; Wang, H.; Yu, Y.; Muller, D. A.; DiSalvo, F. J.; Abruña, H. D. Structurally Ordered Intermetallic Platinum−Cobalt Core−Shell Nanoparticles with Enhanced Activity and Stability as Oxygen Reduction Electrocatalysts. *Nat. Mater.* **2013**, *12* (1), 81−87.

(12) Wang, X. X.; Hwang, S.; Pan, Y.-T.; Chen, K.; He, Y.; Karakalos, S.; Zhang, H.; Spendelow, J. S.; Su, D.; Wu, G. Ordered Pt 3 Co Intermetallic Nanoparticles Derived from Metal−Organic Frameworks for Oxygen Reduction. *Nano Lett.* **2018**, *18* (7), 4163−4171.

(13) Li, J.; Sharma, S.; Liu, X.; Pan, Y.-T.; Spendelow, J. S.; Chi, M.; Jia, Y.; Zhang, P.; Cullen, D. A.; Xi, Z.; Lin, H.; Yin, Z.; Shen, B.;

Muzzio, M.; Yu, C.; Kim, Y. S.; Peterson, A. A.; More, K. L.; Zhu, H.; Sun, S. Hard-Magnet L10-CoPt Nanoparticles Advance Fuel Cell Catalysis. *Joule* **2019**, *3* (1), 124−135.
(14) Liang, J.; Li, N.; Zhao, Z.; Ma, L.; Wang, X.; Li, S.; Liu, X.; Wang, T.; Du, Y.; Lu, G.; Han, J.; Huang, Y.; Su, D.; Li, Q. Tungsten-Doped L1 0 -PtCo Ultrasmall Nanoparticles as a High-Performance Fuel Cell Cathode. *Angew. Chem.* **2019**, *131* (43), 15617−15623.
(15) Wang, T.; Liang, J.; Zhao, Z.; Li, S.; Lu, G.; Xia, Z.; Wang, C.; Luo, J.; Han, J.; Ma, C.; Huang, Y.; Li, Q. Sub-6 nm Fully Ordered L1 0 -Pt−Ni−Co Nanoparticles Enhance Oxygen Reduction via Co Doping Induced Ferromagnetism Enhancement and Optimized Surface Strain. *Adv. Energy Mater.* **2019**, *9* (17), 1803771.
(16) Liang, J.; Zhao, Z.; Li, N.; Wang, X.; Li, S.; Liu, X.; Wang, T.; Lu, G.; Wang, D.; Hwang, B.; Huang, Y.; Su, D.; Li, Q. Biaxial Strains Mediated Oxygen Reduction Electrocatalysis on Fenton Reaction Resistant L1 0 -PtZn Fuel Cell Cathode. *Adv. Energy Mater.* **2020**, *10*, 2000179.
(17) Li, M.; Zhao, Z.; Cheng, T.; Fortunelli, A.; Chen, C.-Y.; Yu, R.; Zhang, Q.; Gu, L.; Merinov, B. V.; Lin, Z.; Zhu, E.; Yu, T.; Jia, Q.; Guo, J.; Zhang, L.; Goddard, W. A.; Huang, Y.; Duan, X. Ultrafine Jagged Platinum Nanowires Enable Ultrahigh Mass Activity for the Oxygen Reduction Reaction. *Science* **2016**, *354* (6318), 1414−1419.
(18) Tian, X.; Zhao, X.; Su, Y. Q.; Wang, L.; Wang, H.; Dang, D.; Chi, B.; Liu, H.; Hensen, E. J. M.; Lou, X. W.; Xia, B. Y. Engineering Bunched Pt-Ni Alloy Nanocages for Efficient Oxygen Reduction in Practical Fuel Cells. *Science* **2019**, *366* (6467), 850−856.
(19) Chen, Y.; Cheng, T.; Goddard, W. A., III Atomistic Explanation of the Dramatically Improved Oxygen Reduction Reaction of Jagged Platinum Nanowires, 50 Times Better than Pt. *J. Am. Chem. Soc.* **2020**, *142* (19), 8625−8632.
(20) Zhao, Z.; Chen, C.; Liu, Z.; Huang, J.; Wu, M.; Liu, H.; Li, Y.; Huang, Y. Pt-Based Nanocrystal for Electrocatalytic Oxygen Reduction. *Adv. Mater.* **2019**, *31* (31), 1808115.
(21) Escudero-Escribano, M.; Malacrida, P.; Hansen, M. H.; Vej-Hansen, U. G.; Velazquez-Palenzuela, A.; Tripkovic, V.; Schiotz, J.; Rossmeisl, J.; Stephens, I. E. L.; Chorkendorff, I. Tuning the Activity of Pt Alloy Electrocatalysts by Means of the Lanthanide Contraction. *Science (Washington, DC, U. S.)* **2016**, *352* (6281), 73−76.
(22) Sharma, S.; Zeng, C.; Peterson, A. A. Face-Centered Tetragonal (FCT) Fe and Co Alloys of Pt as Catalysts for the Oxygen Reduction Reaction (ORR): A DFT Study. *J. Chem. Phys.* **2019**, *150* (4), 041704.
(23) Khorshidi, A.; Violet, J.; Hashemi, J.; Peterson, A. A. How Strain Can Break the Scaling Relations of Catalysis. *Nat. Catal.* **2018**, *1* (4), 263−268.
(24) Strasser, P.; Koh, S.; Anniyev, T.; Greeley, J.; More, K.; Yu, C.; Liu, Z.; Kaya, S.; Nordlund, D.; Ogasawara, H.; Toney, M. F.; Nilsson, A. Lattice-Strain Control of the Activity in Dealloyed Core-Shell Fuel Cell Catalysts. *Nat. Chem.* **2010**, *2* (6), 454−460.
(25) Luo, M.; Guo, S. Strain-Controlled Electrocatalysis on Multimetallic Nanomaterials. *Nat. Rev. Mater.* **2017**, *2*, 17059.
(26) Zhang, S.; Zhang, X.; Jiang, G.; Zhu, H.; Guo, S.; Su, D.; Lu, G.; Sun, S. Tuning Nanoparticle Structure and Surface Strain for Catalysis Optimization. *J. Am. Chem. Soc.* **2014**, *136* (21), 7734−7739.
(27) Bu, L.; Zhang, N.; Guo, S.; Zhang, X.; Li, J.; Yao, J.; Wu, T.; Lu, G.; Ma, J. Y.; Su, D.; Huang, X. Biaxially Strained PtPb/Pt Core/Shell Nanoplate Boosts Oxygen Reduction Catalysis. *Science* **2016**, *354* (6318), 1410−1414.
(28) Hammer, B.; Nørskov, J. K. Electronic Factors Determining the Reactivity of Metal Surfaces. *Surf. Sci.* **1995**, *343* (3), 211−220.
(29) Greegor, R. B.; Lytle, F. W.; Chin, R. L.; Hercules, D. M. Investigation of Supported Cobalt and Nickel Catalysts by X-Ray Absorption Spectroscopy. *J. Phys. Chem.* **1981**, *85* (9), 1232−1235.
(30) Mortensen, J. J.; Hansen, L. B.; Jacobsen, K. W. Real-Space Grid Implementation of the Projector Augmented Wave Method. *Phys. Rev. B: Condens. Matter Mater. Phys.* **2005**, *71* (3), 035109.
(31) Enkovaara, J.; Rostgaard, C.; Mortensen, J. J.; Chen, J.; Dułak, M.; Ferrighi, L.; Gavnholt, J.; Glinsvad, C.; Haikola, V.; Hansen, H. A.; Kristoffersen, H. H.; Kuisma, M.; Larsen, A. H.; Lehtovaara, L.; Ljungberg, M.; Lopez-Acevedo, O.; Moses, P. G.; Ojanen, J.; Olsen, T.; Petzold, V.; Romero, N. A.; Stausholm-Møller, J.; Strange, M.; Tritsaris, G. A.; Vanin, M.; Walter, M.; Hammer, B.; Häkkinen, H.; Madsen, G. K. H.; Nieminen, R. M.; Nørskov, J. K.; Puska, M.; Rantala, T. T.; Schiøtz, J.; Thygesen, K. S.; Jacobsen, K. W. Electronic Structure Calculations with GPAW: A Real-Space Implementation of the Projector Augmented-Wave Method. *J. Phys.: Condens. Matter* **2010**, *22* (25), 253202.
(32) Hjorth Larsen, A.; JØrgen Mortensen, J.; Blomqvist, J.; Castelli, I. E.; Christensen, R.; Dułak, M.; Friis, J.; Groves, M. N.; Hammer, B.; Hargus, C.; Hermes, E. D.; Jennings, P. C.; Bjerre Jensen, P.; Kermode, J.; Kitchin, J. R.; Leonhard Kolsbjerg, E.; Kubal, J.; Kaasbjerg, K.; Lysgaard, S.; Bergmann Maronsson, J.; Maxson, T.; Olsen, T.; Pastewka, L.; Peterson, A.; Rostgaard, C.; SchiØtz, J.; Schütt, O.; Strange, M.; Thygesen, K. S.; Vegge, T.; Vilhelmsen, L.; Walter, M.; Zeng, Z.; Jacobsen, K. W. The Atomic Simulation Environment - A Python Library for Working with Atoms. *J. Phys.: Condens. Matter* **2017**, *29* (27), 273002.
(33) Hammer, B.; Hansen, L. B.; Nørskov, J. K. Improved Adsorption Energetics within Density-Functional Theory Using Revised Perdew-Burke-Ernzerhof Functionals. *Phys. Rev. B: Condens. Matter Mater. Phys.* **1999**, *59* (11), 7413−7421.
(34) Liu, M.; Xin, H.; Wu, Q. Unusual Strain Effect of a Pt-Based L1 0 Face-Centered Tetragonal Core in Core/Shell Nanoparticles for the Oxygen Reduction Reaction. *Phys. Chem. Chem. Phys.* **2019**, *21* (12), 6477−6484.
(35) Nørskov, J. K.; Rossmeisl, J.; Logadottir, A.; Lindqvist, L.; Kitchin, J. R.; Bligaard, T.; Jónsson, H. Origin of the Overpotential for Oxygen Reduction at a Fuel-Cell Cathode. *J. Phys. Chem. B* **2004**, *108* (46), 17886−17892.

https://dx.doi.org/10.1021/jacs.0c08962
J. Am. Chem. Soc. 2020, 142, 19209−19216